




Sulfidation of 2D transition metals (Mo, W, Re, Nb, Ta): thermodynamics, processing, and characterization

Hamed Simchi^{1,*} , Timothy N. Walter¹, Tanushree H. Choudhury¹, Louis Y. Kirkley¹, Joan M. Redwing¹, and Suzanne E. Mohney^{1,*}

¹Department of Materials Science and Engineering and Materials Research Institute, The Pennsylvania State University, University Park, PA 16802, USA

Received: 5 January 2017

Accepted: 23 May 2017

Published online:
30 May 2017

© Springer Science+Business
Media New York 2017

ABSTRACT

Sulfidation of selected transition metal thin films (Mo, W, Re, Nb, Ta) was combined with thermodynamic calculations to study the synthesis of transition metal dichalcogenides (TMDCs) and understand variations among the metals as well as processing atmosphere. Metal seed layers were prepared by DC magnetron sputtering and sulfidized using sulfur vapor and H₂S. Surface chemistry, structure, and morphology of the films were investigated using X-ray photoelectron spectroscopy (XPS), Raman spectroscopy, and atomic force microscopy (AFM), respectively. XPS analysis revealed that after treatment with sulfur vapor ($p(\text{S}_2) = 1\text{--}10$ Torr), Mo, W, and Re films were transformed into MoS₂, WS₂, and ReS₂, respectively. However, Nb and Ta films changed little, and Nb₂O₅ and Ta₂O₅ remained the predominant components. Alternatively, conversion of Nb and Ta films to NbS₂ and TaS₂ was feasible under H₂S. Raman spectroscopy also revealed improved crystallinity for Mo, W, and Re sulfidized under H₂S. Isobaric and isothermal stability diagrams were calculated to identify feasible processing conditions (sulfur partial pressure and temperatures) for the sulfidation of all of the metals, and our findings were in good agreement with the XPS and Raman results. It was found that for Mo, W, and Re a $p(\text{S}_2) = 10^{-5}$ bar is sufficient for the metals to be converted to sulfide phases at 750 °C. On the other hand, due to very high stability of Nb₂O₅ and Ta₂O₅, even at very low $p(\text{O}_2)$, a sulfur partial pressure of $10^3\text{--}10^4$ bar is required to make NbS₂ and TaS₂, respectively. Nevertheless, thermodynamic calculations confirmed that Nb and Ta could be transformed to NbS₂ and TaS₂ under 760 Torr H₂S. AFM analysis revealed very smooth films for MoS₂, WS₂, and NbS₂ films, but dewetting of TaS₂, and ribbons for ReS₂. These results provide guidance for designing new processes for synthesizing 2D TMDCs.

Address correspondence to E-mail: hus21@psu.edu; mohney@ems.psu.edu

Introduction

Two-dimensional transition metal dichalcogenides (2D TMDCs) have attracted interest in recent years due to their unique electrical, optical, and thermal properties resulting from their layered structures. They have strong in-plane covalent bonds and weak van der Waals bonds between layers. As a result, they can be mechanically [1] or chemically [2] exfoliated down to monolayers, as was proposed decades ago.

2D TMDCs have the general formula MX_2 with one layer of a transition metal M sandwiched between two layers of chalcogen atoms X . The main factors determining the electronic structure of TMDCs are the number of d -electrons and coordination environment of the transition metal. Metallic conductivity is obtained when d orbitals are partially filled, e.g., 2H-NbSe₂. Similarly, 2H-MoS₂ and 1T-HfS₂, in which the d orbitals are fully occupied, are semiconductors [3]. Accordingly, a wide range of electronic and magnetic properties can be realized in these materials for applications in superconducting devices (TaS₂ and NbSe₂) [4, 5], light emitting diodes (WS₂) [6], hydrogen evolution (ReS₂) [7], and batteries (VS₂) [8].

Generally, there are three different polytypes identified for TMDCs called 1T, 2H, and 3R based on the presence of 1, 2, or 3 layers in the tetragonal (T), hexagonal (H), and rhombohedral (R) unit cell, respectively. Typically, the 1T phase is a metastable metallic phase, while the 3R and 2H phases are thermodynamically stable. However, density functional theory (DFT) calculations have shown that for ReS₂, the hexagonal phase is unstable [9]. Instead, a distorted 1T structure with buckled S layers and zigzag Re chains is the stable form. Another interesting exception is TaS₂, which is the only TMDC that has 7 polytypes with different stacking sequences along the out-of-plane direction [10]. In this case, polytypes of 1T, 2H, 3R, 4Ha, 4Hc, 4Hb, and 6R have been reported.

Different approaches have been successfully employed to make 2D TMDCs, including chemical/mechanical exfoliation of monolayers from bulk crystals [11, 12], thin film conversion [13], chemical vapor deposition (CVD) [14], metal–organic CVD [15, 16], and atomic layer deposition (ALD) [17]. Among them, sulfidation of oxide or metal seed layers enables a simple approach for the growth of large-area 2D TMDCs [13, 18–20]. Elias et al. [19] have

shown that single and few-layered WS₂ can be grown by deposition of WO₃ on Si/SiO₂ substrates and sulfidizing them at high temperatures (750–950 °C). In another study, Kong et al. [13] fabricated vertically aligned MoS₂/MoSe₂ films by converting ultrathin (<5 nm) Mo films by a sulfidation/selenization process. In a recent study, a MoS₂/WS₂ heterostructure has also been prepared by sequential sputtering of W and Mo, then sulfidizing the layers [21].

By combining semiconducting TMDCs with 2D conductors (e.g., graphene), insulators (e.g., BN), or other TMDC layers (e.g., MoS₂/WSe₂ heterostructure), a broad range of device structures has been proposed. Thus, there is a great motivation to design new processes and structures for next-generation devices. Furthermore, the morphology of TMDCs has a significant influence on their properties and utility for various applications. Though uniform films are desired for electronics, porous or high surface area coatings are beneficial for catalysis.

Thermodynamic calculations will provide insight into the conditions under which a variety of chalcogenides layers can be formed and their stability under specific environmental conditions (pressure, temperature). Therefore, a systematic study on the thermodynamics, processing and characterization of these transition metal dichalcogenides would be beneficial for development of next-generation devices.

In this study, metal seed layers of selected transition metals (Mo, W, Re, Nb, Ta) were prepared by DC magnetron sputtering and sulfidized under atmospheric pressure. The composition, structure, and morphology of the films before and after the sulfidation were investigated using X-ray photoelectron spectroscopy (XPS), Raman spectroscopy, and atomic force microscopy (AFM), respectively. This analysis is supported by thermodynamic calculations to predict the stable phases at different temperatures and partial pressures of sulfur and oxygen, to find a practical pathway for controlled synthesis of TMDCs.

Materials and methods

Oxidized silicon wafers were degreased using acetone, isopropyl alcohol (IPA), and deionized (DI) water. 15-nm Al₂O₃ films were deposited on the wafers using atomic layer deposition (ALD) with

trimethyl aluminum and water as the precursors at 300 °C. Metallic films of Mo, W, Re, Nb, and Ta (>99.95%, Kurt J. Lesker Co.) were deposited on Al₂O₃/SiO₂/Si by DC magnetron sputtering. The sputter chamber was pumped to a base pressure of $\sim 10^{-7}$ Torr. The sputtering gas was argon (Ar), and sputtering rate was 0.1 Å/s. For each run, the target was pre-sputtered for 5 min to clean and condition the surface. Film thickness was 1 nm, determined using a crystal monitor.

The sulfidation process was carried out using an atmospheric pressure furnace. Before loading the samples, the tube was heated to 150 °C to desorb moisture from the walls. Samples (1 cm × 1 cm) were placed on a quartz boat and positioned at the center of the tube. Sulfur powder (99.5%, Alfa Aesar) was placed upstream relative to direction of N₂ gas flow. After loading, the quartz tube was evacuated and then purged for 5 min to minimize the oxygen and water content in the chamber. The oxygen partial pressure in the furnace was measured, while the N₂ gas was flowing, using a DS oxygen probe (Australian Oxytrol Systems) at 750 °C and was found to be $\sim 10^{-17}$ bar.

The sulfidation process was performed at atmospheric pressure in N₂ at a flow rate of 200 sccm. The tube furnace was heated to 750 °C (20 min dwell time) at a rate of 20 °C/min with a 10 min dwell at 380 °C. The temperature of sulfur powder positioned upstream was ~ 200 °C. The quartz tube was cooled to room temperature in about 60 min.

In order to investigate the reaction in a more reactive environment, the sulfidation process was also repeated at 750 °C for 20 min, under 700 Torr of H₂S at a flow rate of 10 sccm.

High-resolution XPS measurements with a 0.1 eV step size were taken to study the core-level binding energy and oxidation states of the films using a Physical Electronics Versaprobe II instrument with monochromatic Al K α X-ray excitation at 20 kV, equipped with dual-beam charge neutralization. Charging offsets were corrected by calibrating the XPS spectrum based on the C 1s peak position (284.8 eV) [22].

Raman spectroscopy was performed using a Horiba LabRam Lucy instrument with a 488 nm laser excitation and 100 \times lens. Atomic force microscopy (AFM) was carried out on a Bruker Icon scanning probe microscope in the PeakForce Tapping mode to provide topographic information about the samples.

The AFM tip was a ScanAsyst air probe with a nominal tip radius of ~ 2 nm and spring constant of 0.4 N/m. Images of a 10 μm × 10 μm area were collected using PeakForce Tapping mode with a peak-force set point of 0.5 nN.

Thermodynamic calculations were performed using the HSC Chemistry software version 8.0 to predict the conditions at which sulfides or oxides are stable. Through the minimization of Gibbs free energy, stability diagrams were calculated at atmospheric pressure holding the partial pressure of one species constant (isobaric diagrams). In addition, isothermal diagrams were generated using the reaction equations. Species included are listed in Table S1. The measured oxygen partial pressure in our furnace was 10^{-17} bar, and our typical processing temperature was 750 °C.

Results and discussion

XPS analysis

Figure 1 shows the high-resolution XPS scans of different films, before and after sulfidation with sulfur vapor. Most of the patterns show an asymmetric line shape, suggesting the presence of mixed oxidation states. Peaks were fit by Gaussian–Lorentzian curves satisfying the following constraints: a) the doublets intensities have the ratio of 4:3, 3:2, and 2:1 for the electrons coming from *f*, *d*, and *p* orbitals, respectively; b) each doublet has equal full width at half maximum (FWHM); and c) the spin orbit splitting of the doublets are matched with database [22, 23]. Peak positions for the core levels of each compound are summarized in Table 1 and compared with the NIST database for identification [23].

Figure 1a shows the high-resolution scan of Mo 3d doublet core levels. The peak fitting shown in Fig. 1a resolved that the as-deposited films contain three oxidation states of Mo⁶⁺, Mo⁵⁺, and Mo⁴⁺, corresponding to MoO₃, Mo₂O₅, and MoO₂, respectively. Sulfidizing the Mo films resulted in the shift of both Mo 3d_{5/2} and Mo 3d_{3/2} core levels to lower energy values. As a result, most of the film transformed to the MoS₂ phase with a small contribution from MoO_{3-x}. The MoO_{3-x} might come from the incomplete sulfidation of Mo films, or from surface oxides formed after sulfidation but before the samples were analyzed by XPS.

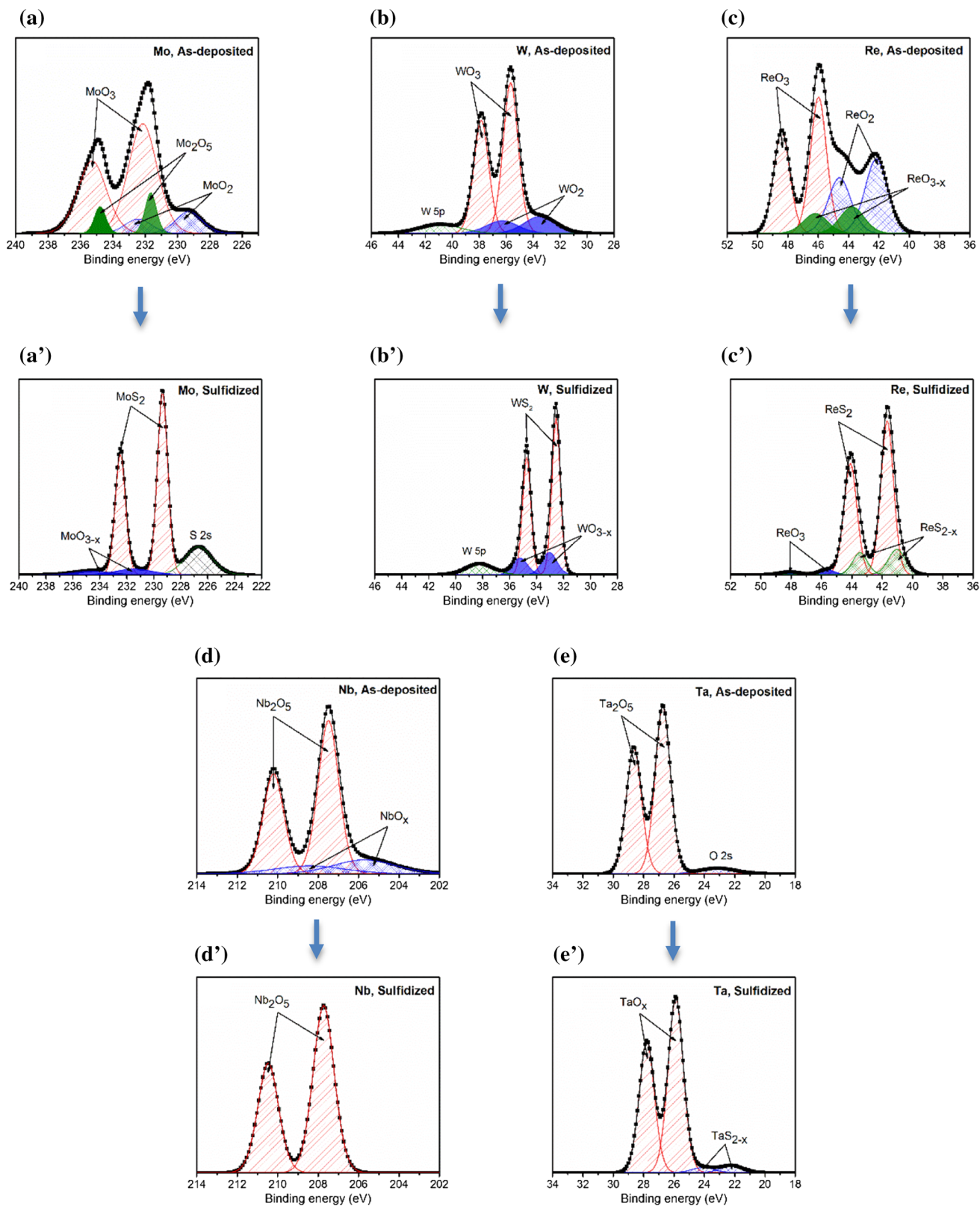


Figure 1 XPS analysis of **a, a'** Mo, **b, b'** W, **c, c'** Re, **d, d'** Nb, and **e, e'** Ta before and after the sulfidation with sulfur vapor. In each case, peak fittings are also shown determining different oxidation states (chemical bonding).

Table 1 Core-level binding energies of different films, before and after sulfidation

Core level	Binding energy (eV)	
	As-deposited	Sulfidized
Mo 3d _{5/2}	232.15, 231.65, 229.31	229.35, 231.47
W 4f _{7/2}	35.68, 32.79	32.55, 33.04
Re 4f _{7/2}	45.98, 43.77, 42.17	41.67, 41.03, 45.66
Nb 3d _{5/2}	207.49, 205.72	207.73
Ta 4f _{7/2}	26.78	25.91, 22.21

High-resolution scans of the W 4f doublet core levels (Fig. 1b) show that the as-deposited W film produces an asymmetric line shape indicating the presence of mixed oxidation states. Peaks located at energies of 35.68 and 32.79 eV were identified as the 4f_{7/2} peaks of the WO₃ and WO₂ phases, respectively. Sulfidized films reveal WS₂ with a minor contribution from WO_{3-x}.

For the Re films, several oxidation states of ReO₃, ReO_{3-x}, and ReO₂ were found with peaks located at 45.98, 43.77, and 42.17 eV, respectively (Fig. 1c). After sulfidation, ReS₂ was present with small contribution from a non-stoichiometric sulfide (ReS_{2-x}) and ReO₃. Again, a small contribution from oxides might be due to incomplete sulfidation, or surface oxidation of ReS₂ films after sulfidation and removal of the samples from the furnace.

The XPS analysis of the Nb 3d region is shown in Fig. 1d. It can be seen that Nb₂O₅ (207.49 eV) is the main phase at the surface with a small contribution from sub-stoichiometric oxides with peaks located at lower binding energies (205.72 eV). After sulfidation, peaks from the sub-oxide vanished, and only Nb₂O₅ was detectable at the surface. No evidence was found for the formation of any Nb-sulfide phase, with $p(S_2) = 1\text{--}10$ Torr in this study. Therefore, these phases did not form or might be transformed to the more stable oxide phase during the storage/handling of samples. The 3d_{5/2} peak of the NbS₂ phase would be expected at 203.5 eV [23], which was not observed in our samples.

Similar to Nb, Ta₂O₅ is the main phase detected for the sputtered Ta films (Fig. 1e). After sulfidation, peaks were slightly shifted to lower binding energies due to partial reduction of tantalum oxide. In addition, small peaks can be identified at 22.21 and 24.11 eV corresponding to the 4f_{7/2} and 4f_{5/2} peaks of TaS_{2-x}, respectively.

Raman spectroscopy

Figure S1 shows the Raman spectra for Mo, W, and Re films after sulfidation. For the sulfidized Mo films (Fig. S1a), Raman peaks were observed at 403.4 and 380.3 cm⁻¹, corresponding to A_{1g} and E_{2g} vibrations of 2H-MoS₂. The 23.1 cm⁻¹ difference between the two modes suggests a three-layer thickness for the MoS₂ films [24].

Similarly, Raman spectra of the WS₂ films show A_{1g} and E_{2g} peaks of 2H-WS₂ located at 419.3 and 355.7 cm⁻¹, respectively (Fig. S1b). The film thickness can be estimated to be ~3 layers based on the 63.6 cm⁻¹ difference between the two modes [25]. It should be noted that for both MoS₂ and WS₂ films, the high intensity ratio of E_{2g}/A_{1g} indicates a noticeable in-plane vibration (E_{2g}) over the out-of-plane vibration (A_{1g}). Therefore, the growth mode for MoS₂ and WS₂ films was mainly horizontal. This observation is in agreement with the work done by Jung et al. [20], which reported the horizontal (vertical) growth of MoS₂ or WS₂ when the metal seed layer thickness is ≤0.5 nm (≥3–4 nm).

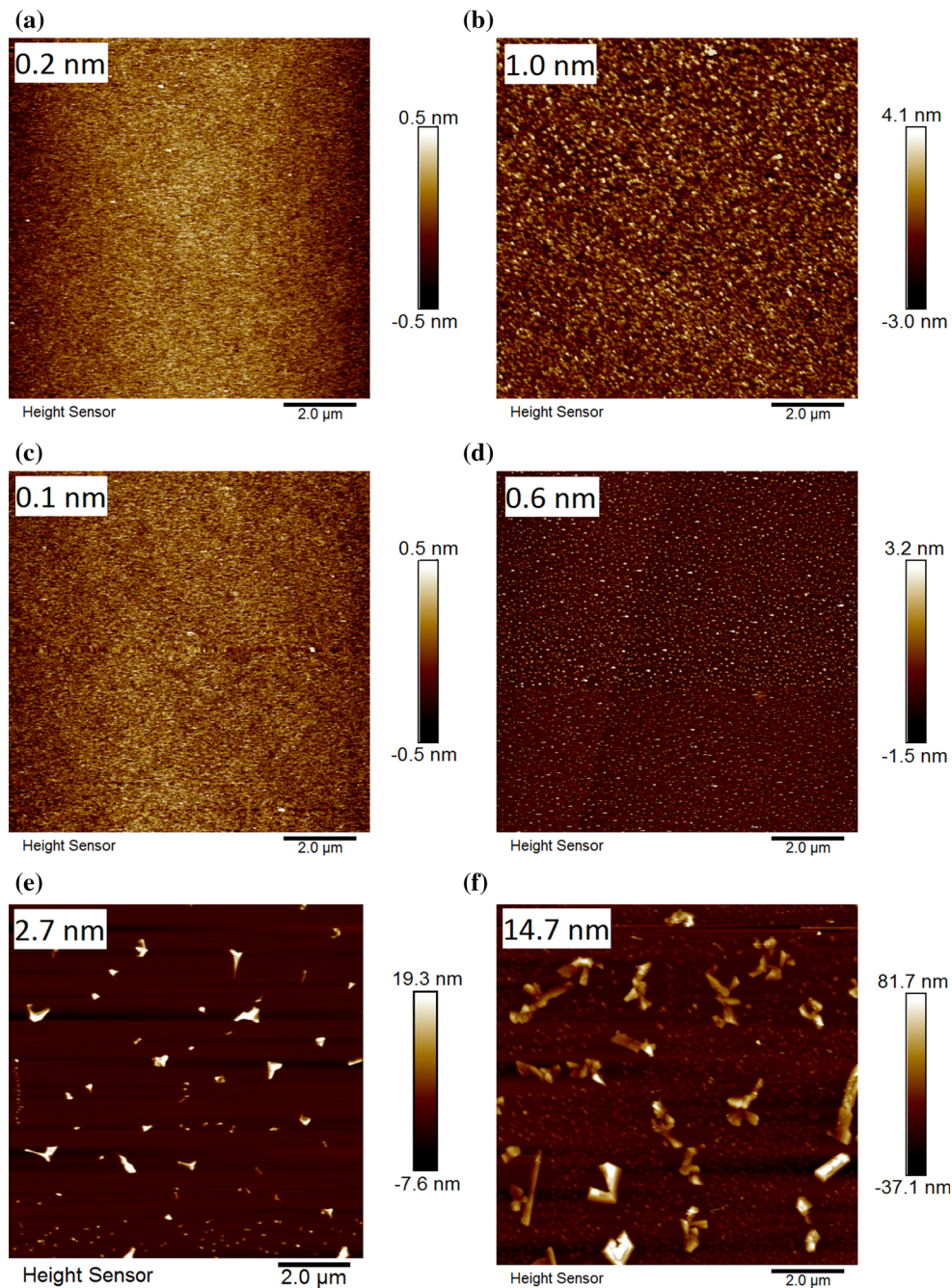
For the sulfidized Re films (Fig. S1c), Raman spectra had a much lower signal-to-noise ratio, and many of the peaks expected for ReS₂ were buried under peaks of Al₂O₃ or background. This situation might arise from low crystallinity of the films, incomplete transformation to ReS₂, or coverage of ReS₂ crystals over only a small fraction of the substrate.

Raman spectra for the Nb and Ta films (Fig. S1 d, e) do not show any obvious peaks, besides the Al₂O₃, again indicating that sulfide phases were not formed in these samples under 1–10 Torr $p(S_2)$.

AFM analysis

Atomic force microscopy (AFM) was used to analyze the topography of the films, before and after the sulfidation. Figures 2 and S2 show that except for Re, all of the sputtered films are very smooth with RMS roughness <0.2 nm. Very good wetting of transition metals on the alumina surface correlates with the interaction between metal *d* orbitals and oxygen *p* orbitals resulting in metal (*d*)–oxygen (*p*) bonding. The strength of metal-oxide bond decreases from early transition metals to noble metals where the *d*-band occupancy increases [26]. Therefore, it is not surprising that Re films would have poor wetting

Figure 2 AFM analysis of **a**, **b** Mo, **c**, **d** W, and **e**, **f** Re films before and after sulfidation. RMS roughness values are also shown for comparison.



(higher contact angle) compared to other transition metals in this study.

In fact, a quite different morphology consisting of flakes and islands was observed for the Re films. In this case, Re atoms bond more strongly to each other than to the substrate, leading to the formation of three-dimensional adatom clusters or islands. Similar structures have been reported by Cazzanelli et al. [27]

for ReO_3 films grown on quartz, glass, and indium tin oxide (ITO) substrates. Oh et al. [28] have also shown that islands with diameter >100 nm form by high-temperature DC sputtering of Re films on epi-ready Al_2O_3 (sapphire).

After sulfidation, rather dissimilar morphologies were obtained for different transition metals. For the Mo films, as mentioned above, MoS_2 is the

Table 2 Different oxide and sulfide phases included in the thermodynamic calculations

Metal	Shown on phase diagram		Additional phases in HSC database
	Oxides	Sulfides	
Mo	MoO ₂ , Mo ₄ O ₁₁ , Mo ₈ O ₂₃ , Mo ₉ O ₂₆ , MoO ₃	MoS ₂ , Mo ₂ S ₃	MoS ₃
W	WO ₂ , WO ₃	WS ₂ , WS ₃	WO _{2.72} , W ₃ O
Re	ReO ₂	NA	ReO ₃ , Re ₂ O ₃ , Re ₂ O ₇ , ReS ₂ , ReS ₃ , Re ₂ S ₇
Nb	NbO, NbO ₂ , Nb ₂ O ₅	NbS, NbS ₂	NbS _{1.65}
Ta	Ta ₂ O ₅	NA	TaS ₂ , TaS ₃

References for each phase are provided in the supplementary section, Table S1

predominant phase. In this case, RMS roughness is increased to ~ 1 nm with a few bright (higher z height) spots (Fig. 2b). Similarly, a fairly smooth structure, with RMS roughness of 0.6 nm, and localized higher z spots were found for the sulfidized W films (Fig. 2d), which formed WS₂.

Figure 2f shows that during sulfidation, Re islands coalesce together, forming very large ReS₂ ribbons of >1 μm in length, with RMS roughness of 14.7 nm. These rearrangements happen when the small clusters move randomly and join larger crystals (Ostwald ripening). Very small nanoribbons can still be detected on the surface, but areas surrounding the big ribbons are completely depleted. He et al. [29] have shown that the morphology of CVD-grown ReS₂ varies significantly with time. While very short growth time results in the formation of hexagonal flakes, increasing the time leads to thinning of the flakes and formation of ReS₂ nanoribbons. The difference between the morphology of ReS₂ and other TMDCs might be due to the different crystal structure of ReS₂. Initial formation of Re islands before sulfidation could also promote the growth of ribbons instead of uniform films.

Figure S2 shows that Nb films subjected to sulfur vapor were still pretty smooth with a slight increase in RMS roughness value to 0.6 nm. Similarly, Ta films subjected to sulfur vapor (Fig. S2) were very smooth with a surface roughness of only 0.2 nm. As revealed by XPS analysis (Fig. 2d', e'), niobium sulfide and tantalum sulfide did not form.

Thermodynamic calculations

The different solid phases considered in the calculations of thermodynamic stability diagrams are summarized in Table 2 (references provided in the

supplementary section). They were chosen based on the binary M–O and M–S (M = Mo, W, Re, Nb, Ta) phase diagrams [30]. In some cases, other phases that are not shown on the phase diagram but have been reported in the literature [31, 32] and their enthalpy, entropy, and Gibbs free energy values available in the HSC database were also added for a more complete analysis.

Isobaric (Fig. 3) and isothermal (Fig. S3) stability diagrams were calculated in order to find the feasible process conditions for the sulfidation of oxide films to form TMDCs. For the isobaric stability diagrams, $p(\text{O}_2)$ was set to 10^{-17} bar, the measured value in our furnace. Isothermal diagrams were calculated at typical processing temperature of 750 °C. In each case, the most stable phases (lowest Gibbs free energy) were found for a range of sulfur partial pressures and temperatures (isobaric) or combination of sulfur and oxygen partial pressure (isothermal). On the stability diagrams, lines and points represent conditions for equilibria between two and three condensed phases, respectively.

In Fig. 3, red spots show the process conditions for our sulfidation experiments, and dotted lines show an example to find the $p(\text{S}_2)$ required to convert the oxide to sulfide at processing temperature of 750 °C. For the Mo films (Fig. 3a), MoO₃ was found to be the main component favored at room temperature. The oxide phase is favored to transform to MoS₂ at $T > 450$ °C at $p(\text{S}_2) = 10^{-4}$ bar. This prediction is in agreement with XPS results (Fig. 1b) showing that MoS₂ is the dominant phase after sulfidation. In fact, $p(\text{S}_2)$ of only 10^{-8} bar is required to convert the oxide to sulfide at 750 °C.

It should be noted that MoS₃ is not shown on the Mo–S phase diagram [30], but its thermodynamic data has been reported in the literature [32] and was included in our calculations. Nevertheless, conflicting

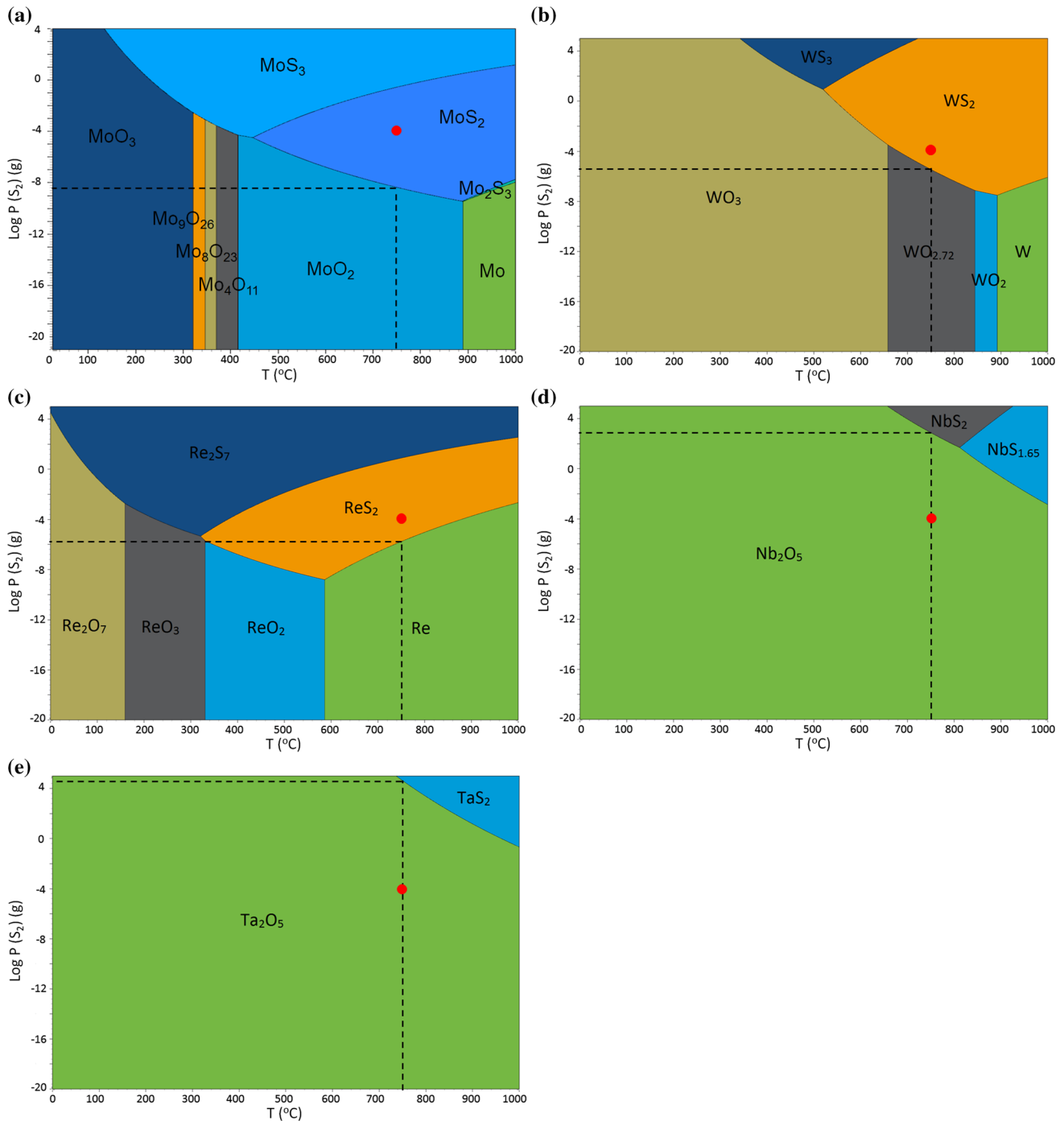


Figure 3 Calculated isobaric stability diagrams for different transition metal-S-O systems at $p(\text{O}_2) = 10^{-17}$ bar: **a** Mo, **b** W, **c** Re, **d** Nb, and **e** Ta. Dotted lines show an example to find

the $p(\text{S}_2)$ required to convert the oxide, or in case of Re the metal, to sulfide for a typical processing temperature of $750 \text{ }^\circ\text{C}$. Red spots show the process conditions in our experiments.

information in the literature leaves us with some uncertainty about MoS_3 , even though the available thermodynamic data suggest it could form at low temperatures or high $p(\text{S}_2)$.

Thermodynamic calculations for the W films are shown in Fig. 3b. Similar to Mo, it was found that WO_3 is the most stable phase at room temperature (Fig. 1b). During sulfidation, it is favored to

transform to WS_2 at >650 °C (Fig. 3b). This finding is in agreement with our XPS results and the W–S phase diagram [30]. Dotted lines in Fig. 3b show that a sulfur partial pressure as low as 10^{-5} bar can favor WS_2 at 750 °C. WS_3 is reported on the W–S phase diagram, and thermodynamic data are available in the literature [32]. However, its reported amorphous structure leaves some uncertainty about WS_3 .

There is no phase diagram available for the Re–S system, but thermodynamic values for the ReS_2 , ReS_3 , and Re_2S_7 were available in the HSC database. Figure 3c shows the isobaric stability diagram for the Re films. Thermodynamics predict that formation of ReS_2 is favored at $T \geq 350$ °C. This observation is in good agreement with XPS results indicating that ReS_2 would form in such a sulfidizing environment. Previous studies have also shown that ReS_2 is the stable form in the Re–S system and forms by heating the Re_2S_7 at 150 °C [33, 34].

In the Nb–S system, only the thermodynamic values for NbS, $NbS_{1.65}$, and NbS_2 were found in the literature. Formation of other sulfide phases such as Nb_3S_4 , $Nb_{1+x}S_2$ [35], Nb_2S_3 [36], and Nb_4S_7 has been reported but are not shown in the Nb–S phase diagram [30] and was not included here. For the Nb films (Fig. 3d), Nb_2O_5 is very stable at room temperature (as shown in Fig. 1d) with little change until ~ 800 °C. This calculation matches our XPS results in which only Nb_2O_5 was found after sulfidation.

Early studies on the sulfidation of Nb films showed that, due to high stability of the Nb_2O_5 , very high sulfur pressure of up to 6 atm and temperatures >750 °C were required to form the NbS_2 phase [37]. Also, in a recent study by Dash et al. [38], the 3R- NbS_2 phase was obtained by the sulfidation reaction of Nb films in which the sulfur source was placed adjacent to the Nb films at the center of the hot zone, to obtain very high sulfur chemical potential. The dotted line in Fig. 3d shows that a sulfur partial pressure of $\sim 10^3$ bar is required to make NbS_2 at 750 °C.

There is no Ta–S phase diagram available in the literature. However, the ternary phase diagram of Li–Ta–S shows the TaS, TaS_2 , and TaS_3 phases at 27 °C [30]. It was also shown in an early study by Jellinek [39] that TaS_3 , five different phases of TaS_2 , and three other stoichiometries of sulfides ($Ta_{1+x}S_2$) may form in the Ta–S system.

Figure 3e shows that similar to Nb, the oxide of Ta would be the stable phase at room temperature and is

stable until very high $p(S_2)$. In fact, a sulfur partial pressure of 10^4 bar is required to convert it to TaS_2 at 750 °C. This report is consistent with our XPS results revealing that Ta_2O_5 is the dominant phase after sulfidation.

In summary, it can be seen that for Mo, W, and Re a $p(S_2) = 10^{-5}$ bar is sufficient for the metals to be converted to sulfide phases at 750 °C. On the other hand, due to very high stability of Nb_2O_5 and Ta_2O_5 , even at such a low $p(O_2)$, a sulfur partial pressure of 10^3 – 10^4 bar is required to make NbS_2 and TaS_2 , respectively. Isothermal stability diagrams (Fig. S3) calculated at 750 °C demonstrate how different sulfide/oxide phases can be obtained by tuning the $p(S_2)$ and $p(O_2)$. Again, they confirm that extremely low $p(O_2)$ or very high $p(S_2)$ is required to make sulfides of Nb and Ta. These stability diagrams can therefore guide experiments for the controlled processing of TMDCs.

H₂S treatment

An alternate way to prepare TMDCs would be to use reducing agents, e.g., H_2 , as a carrier gas, or more reactive environment, e.g., H_2S , to convert highly stable Nb_2O_5 and Ta_2O_5 to sulfide phases. HSC Chemistry software will not create a stability diagram when there are more than three elements in a system, so another approach is to find the equilibrium composition of each phase for a closed system. Although the furnace is actually purged with H_2S and the volatile reaction products are swept away, H_2S is continuously supplied to the system, so the conditions are close enough to provide reasonable guidance.

For the Nb films (Fig. 4a), Nb_2O_5 is favored to transform to NbS_2 even at room temperature under 750 Torr H_2S , although it is possible that kinetics would not permit it. On the other hand, due to high stability of Ta_2O_5 , TaS_2 is favored to form at >300 °C (Fig. 4b). Therefore, the sulfidation process was repeated at 750 °C for 20 min under 700 Torr of H_2S at a flow rate of 100 sccm.

Figure 4c shows the high-resolution XPS scan of the Nb 3d doublet core levels after H_2S treatment. The peak fitting shown in Fig. 4c resolved that after H_2S treatment, most of the film transformed to the NbS_2 phase with some contribution from sub-stoichiometric oxides or oxysulfides. These contributions might come from the incomplete sulfidation of Nb

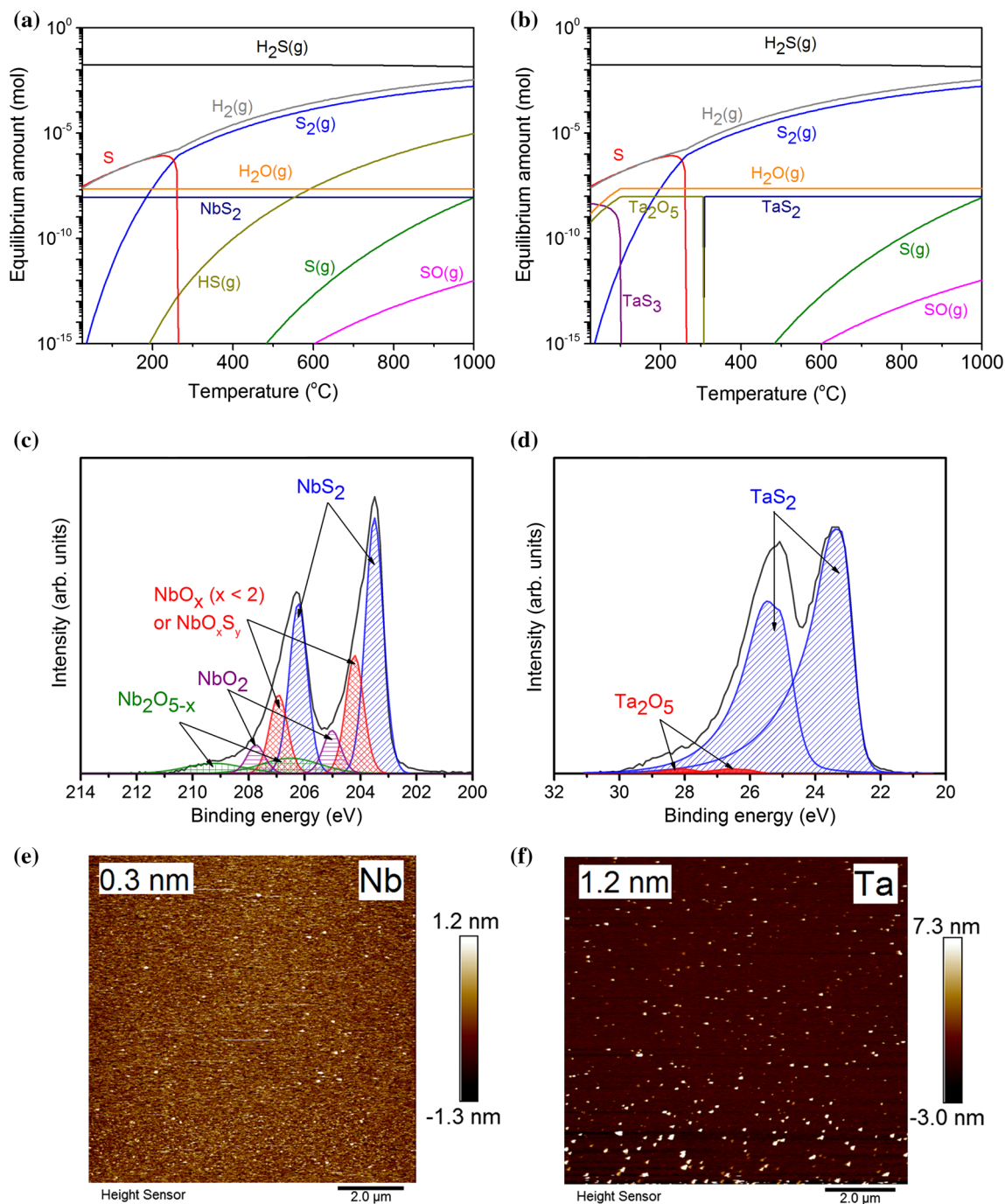


Figure 4 **a, b** Thermodynamic plots showing the expected amounts of products at equilibrium for the sulfidation of **a** Nb₂O₅ and **b** Ta₂O₅ as a function of temperature, under 700 Torr H₂S. Since the starting oxidized films were

~1 cm × 1 cm × 1 nm in size, the initial number of moles of the metal reactants was in the range 10⁻⁸–10⁻⁹ mol. **c, d** XPS analysis of Nb and Ta after sulfidation with H₂S at 750 °C. **e, f** AFM analysis of **e** Nb and **f** Ta films after sulfidation with H₂S.

films or surface oxides formed after sulfidation but before the samples were analyzed by XPS.

The XPS analysis of the Ta 4f region after H₂S treatment is shown in Fig. 4d. It can be seen that TaS₂

(4f_{7/2}: 23.23 eV) is the main phase at the surface with only a small contribution from Ta₂O₅ (4f_{7/2}: 26.19 eV). No evidence was found for the formation of any sub-stoichiometric oxide or sulfide phases.

XPS analysis of Mo, W, and Re films after H₂S treatment is presented in Fig. S4. Compared to films sulfidized with sulfur powder, sharper peaks of sulfides with negligible peaks of oxides can be detected. Thus, phase transformation to MoS₂, WS₂, and ReS₂ was more complete after H₂S treatment.

Figures S5 shows the results of Raman spectroscopy for the Nb and Ta films. Peaks located at ~302 and ~435 cm⁻¹ were identified as the active modes of a hydrated Al₂O₃ substrate [40], which makes the precise recognition of phases challenging. Still, for the NbS₂, Raman peaks at ~382 and ~150 can be assigned to the A₁ and two-phonon scattering modes of 3R-NbS₂, respectively [41, 42]. However, weak peak intensities suggest poor crystallinity and incomplete conversion to NbS₂, as observed from XPS analysis (Fig. 4c). Expected positions for other modes are shown with arrows in Fig. S5d, which were mostly obscured by the Al₂O₃ signal.

Raman spectra for the Ta films, after sulfidation with H₂S, are shown in Fig. S5e. No obvious peaks were observed and only Al₂O₃ was detectable. Raman peaks were expected to be present at 100, 243, 306 and 381 cm⁻¹ [43] as noted in Fig. S5. However, previous studies have shown that due to formation of charge density waves (CDW) in TaS₂, most of the Raman modes vanish at temperatures close to room temperature [43–45], particularly in films <4 nm [46].

AFM of Nb and Ta films after sulfidation with H₂S are shown in Fig. 4e, f, respectively. For the Nb films, a very smooth morphology with a few bright (higher z height) spots was obtained. The RMS roughness was <0.3 nm. Conversely, Fig. 4f shows that sulfidation of Ta with H₂S causes dewetting of the films, forming islands, with average size ~200 nm.

To best of our knowledge, this is the first report on converting Re, Nb, and Ta films to sulfides using the H₂S environment. These results indicate that H₂S treatment can be a practical pathway to convert even highly stable Nb and Ta oxides to sulfides. Furthermore, optimization of the process could fine tune the crystallinity and composition of the films.

Conclusions

In this study, sulfidation of transition metals (Mo, W, Re, Nb, Ta), deposited by DC magnetron sputtering and sulfidized in sulfur vapor and H₂S, were investigated. It was found that all of the as-deposited metal

films were fully or partially oxidized during the storage or handling in the laboratory environment. XPS analysis revealed that Mo, W, and Re films were transformed to MoS₂, WS₂, and ReS₂ phases. In contrast, sulfidation of Nb and Ta films was challenging, and Nb₂O₅ and Ta₂O₅ were still the dominant phases after the sulfur treatment.

AFM analysis of the surface topographies revealed that except Re, all of the sputtered films were very smooth (RMS roughness < 0.2 nm). After sulfidation, MoS₂ and WS₂ were smooth, but very large ribbons of ReS₂ formed.

Thermodynamic calculations were made to predict the conditions (sulfur partial pressure, oxygen partial pressure and temperatures) at which sulfides are stable. It was found that oxides of Mo, W, and Re are favored to transform into sulfides (even at $p(\text{S}_2) = 10^{-5}$ bar), in good agreement with the XPS. On the other hand, oxides of Nb and Ta are quite stable (until $p(\text{S}_2) > 10^3$ bar), making it difficult to form sulfides.

Thermodynamic calculations under equilibrium condition suggested that sulfidation of Nb₂O₅ and Ta₂O₅ is feasible in H₂S. This prediction was verified by repeating the sulfidation process under 700 Torr H₂S. XPS analysis revealed that Nb₂O₅ and Ta₂O₅ were transformed to NbS₂ and TaS₂, respectively. Raman spectroscopy showed peaks corresponding to 3R-NbS₂. In contrast, no peaks were detected for TaS₂. AFM analysis showed very smooth NbS₂, but island growth for TaS₂.

These results in addition to stability diagrams presented in this work can guide future experiments for finding new functionality by creating heterostructures or by alloying/doping TMDCs.

Associated content

Supporting information

“This material is available free of charge via the Internet at doi:10.1007/s10853-017-1228-x”.

Raman spectra for the Mo, W, Re, Nb, and Ta films after sulfidation with sulfur vapor (Fig. S1), AFM analysis of Nb, Ta films before and after the sulfur treatment (Fig. S2), calculated isothermal stability diagrams for different transition metal–S–O systems at 750 °C (Fig. S3), XPS spectra for Mo, W, and Re films after sulfidation with H₂S (Fig. S4), and Raman spectra for Mo, W, Re, Nb, and Ta films after

sulfidation with H₂S (Fig. S5), A list of all species included in thermodynamic calculations and references for each species at the appropriate temperature range (Table S1).

Acknowledgements

The authors acknowledge the support by the National Science Foundation (NSF) through EFRI-1433378.

Electronic supplementary material: The online version of this article (doi:[10.1007/s10853-017-1228-x](https://doi.org/10.1007/s10853-017-1228-x)) contains supplementary material, which is available to authorized users.

References

- Frindt RF (1966) Single crystals of MoS₂ several molecular layers thick. *J Appl Phys* 37:1928–1932. doi:[10.1063/1.1708627](https://doi.org/10.1063/1.1708627)
- Joensen P, Frindt RF, Morrison SR (1986) Single-layer MoS₂. *Mater Res Bull* 21:457–461. doi:[10.1016/0025-5408\(86\)90011-5](https://doi.org/10.1016/0025-5408(86)90011-5)
- Wilson JA, Yoffe AD (1969) The transition metal dichalcogenides discussion and interpretation of the observed optical, electrical and structural properties. *Adv Phys* 18:193–335. doi:[10.1080/00018736900101307](https://doi.org/10.1080/00018736900101307)
- Ugeda MM, Bradley AJ, Zhang Y et al (2015) Characterization of collective ground states in single-layer NbSe₂. *Nat Phys* 12:92–97. doi:[10.1038/nphys3527](https://doi.org/10.1038/nphys3527)
- Sipos B, Kusmartseva AF, Akrap A et al (2008) From Mott state to superconductivity in 1T-TaS₂. *Nat Mater* 7:960–965. doi:[10.1038/nmat2318](https://doi.org/10.1038/nmat2318)
- Baugher BWH, Churchill HOH, Yang Y, Jarillo-Herrero P (2014) Optoelectronic devices based on electrically tunable p–n diodes in a monolayer dichalcogenide. *Nat Nanotechnol* 9:262–267. doi:[10.1038/nnano.2014.25](https://doi.org/10.1038/nnano.2014.25)
- Fujita T, Ito Y, Tan Y et al (2014) Chemically exfoliated ReS₂ nanosheets. *Nanoscale* 6:12458–12462. doi:[10.1039/c4nr03740e](https://doi.org/10.1039/c4nr03740e)
- Jing Y, Zhou Z, Cabrera CR, Chen Z (2013) Metallic VS₂ monolayer: a promising 2D anode material for lithium ion batteries. *J Phys Chem C* 117:25409–25413. doi:[10.1021/jp410969u](https://doi.org/10.1021/jp410969u)
- Tongay S, Sahin H, Ko C et al (2014) Monolayer behaviour in bulk ReS₂ due to electronic and vibrational decoupling. *Nat Commun* 5:3252. doi:[10.1038/ncomms4252](https://doi.org/10.1038/ncomms4252)
- Enomoto H, Kawano T, Kawaguchi M et al (2004) Van der Waals growth of thin TaS₂ on layered substrates by chemical vapor transport technique. *Jpn J Appl Phys* 43:L123–L126. doi:[10.1143/JJAP.43.L123](https://doi.org/10.1143/JJAP.43.L123)
- Radisavljevic B, Radenovic A, Brivio J et al (2011) Single-layer MoS₂ transistors. *Nat Nanotechnol* 6:147–150. doi:[10.1038/nnano.2010.279](https://doi.org/10.1038/nnano.2010.279)
- Nicolosi V, Chhowalla M, Kanatzidis MG et al (2013) Liquid exfoliation of layered materials. *Science* 340:1226419. doi:[10.1126/science.1226419](https://doi.org/10.1126/science.1226419)
- Kong D, Wang H, Cha JJ et al (2013) Synthesis of MoS₂ and MoSe₂ films with vertically aligned layers. *Nano Lett* 13:1341–1347. doi:[10.1021/nl400258t](https://doi.org/10.1021/nl400258t)
- Zhan Y, Liu Z, Najmaei S et al (2012) Large-area vapor-phase growth and characterization of MoS₂ atomic layers on a SiO₂ substrate. *Small* 8:966–971. doi:[10.1002/sml.201102654](https://doi.org/10.1002/sml.201102654)
- Kang K, Xie S, Huang L et al (2015) High-mobility three-atom-thick semiconducting films with wafer-scale homogeneity. *Nature* 520:656–660. doi:[10.1038/nature14417](https://doi.org/10.1038/nature14417)
- Eichfeld SM, Hossain L, Lin Y-C et al (2015) Highly scalable, atomically thin WSe₂ grown via metal–organic chemical vapor deposition. *ACS Nano* 9:2080–2087. doi:[10.1021/nn5073286](https://doi.org/10.1021/nn5073286)
- Jin Z, Shin S, Kwon DH et al (2014) Novel chemical route for atomic layer deposition of MoS₂ thin film on SiO₂/Si substrate. *Nanoscale* 6:14453–14458. doi:[10.1039/c4nr04816d](https://doi.org/10.1039/c4nr04816d)
- Gaur APS, Sahoo S, Ahmadi M et al (2013) Optical and vibrational studies of partially edge-terminated vertically aligned Nanocrystalline MoS₂ thin films. *J Phys Chem C* 117:26262–26268. doi:[10.1021/jp407377g](https://doi.org/10.1021/jp407377g)
- Eliás AL, Perea-López N, Castro-Beltrán A et al (2013) Controlled synthesis and transfer of large-area WS₂ sheets: from single layer to few layers. *ACS Nano* 7:5235–5242. doi:[10.1021/nn400971k](https://doi.org/10.1021/nn400971k)
- Jung Y, Shen J, Liu Y et al (2014) Metal seed layer thickness-induced transition from vertical to horizontal growth of MoS₂ and WS₂. *Nano Lett* 14:6842–6849. doi:[10.1021/nl502570f](https://doi.org/10.1021/nl502570f)
- Woods JM, Jung Y, Xie Y et al (2016) One-step synthesis of MoS₂/WS₂ layered heterostructures and catalytic activity of defective transition metal dichalcogenide films. *ACS Nano* 10:2004–2009. doi:[10.1021/acsnano.5b06126](https://doi.org/10.1021/acsnano.5b06126)
- Crist BV (2000) Handbook of monochromatic XPS spectra by B. John Wiley and Sons Ltd., England
- Naumkin AV, Kraut-Vass A, Gaarenstroom SW, Powell CJ (2012) NIST X-ray photoelectron spectroscopy (XPS) database, version 4.1
- Li H, Zhang Q, Yap CCR et al (2012) From bulk to monolayer MoS₂: evolution of Raman scattering. *Adv Funct Mater* 22:1385–1390. doi:[10.1002/adfm.201102111](https://doi.org/10.1002/adfm.201102111)

- [25] Berkdemir A, Gutiérrez HR, Botello-Méndez AR et al (2013) Identification of individual and few layers of WS₂ using Raman Spectroscopy. *Sci Rep* 3:1–8. doi:[10.1038/srep01755](https://doi.org/10.1038/srep01755)
- [26] Lazzari R, Jupille J (2005) Wetting and interfacial chemistry of metallic films on the hydroxylated α -Al₂O₃ (0001) surface. *Phys Rev B Condens Matter Mater Phys* 71:1–13. doi:[10.1103/PhysRevB.71.045409](https://doi.org/10.1103/PhysRevB.71.045409)
- [27] Cazzanelli E, Castriota M, Marino S et al (2009) Characterization of rhenium oxide films and their application to liquid crystal cells. *J Appl Phys* 105:114904. doi:[10.1063/1.3138812](https://doi.org/10.1063/1.3138812)
- [28] Oh S, Hite DA, Cicak K et al (2006) Epitaxial growth of rhenium with sputtering. *Thin Solid Films* 496:389–394. doi:[10.1016/j.tsf.2005.09.091](https://doi.org/10.1016/j.tsf.2005.09.091)
- [29] He X, Liu F, Hu P et al (2015) Chemical vapor deposition of high-quality and atomically layered ReS₂. *Small* 11:5423–5429. doi:[10.1002/sml.201501488](https://doi.org/10.1002/sml.201501488)
- [30] Villars P, Okamoto H, Cenzual K (2006) ASM alloy phase diagrams database. <http://www1.asminternational.org/AsmEnterprise/APD>. 990389
- [31] Villars P, Calvert LD (1986) Pearson's handbook of crystallographic data for intermetallic phases. Am Soc Met. doi:[10.1002/crat.2170221117](https://doi.org/10.1002/crat.2170221117)
- [32] Mills KC (1974) Thermodynamic data for inorganic sulphides. Selenides and Tellurides. Butterworth & Co Ltd, London
- [33] Sidgwick NV (1950) The chemical elements and their compounds. Clarendon Press, Oxford, Glasgow
- [34] Wildervanck JC, Jellinek F (1971) The dichalcogenides of technetium and rhenium. *J Less-Common Met* 24:73–81. doi:[10.1016/0022-5088\(71\)90168-8](https://doi.org/10.1016/0022-5088(71)90168-8)
- [35] Hodouin D (1975) The standard free energy of formation of nonstoichiometric niobium sulfides. *Metall Trans B* 6:223–228. doi:[10.1007/BF02913563](https://doi.org/10.1007/BF02913563)
- [36] Jellinek F, Brauer G, Muller H (1960) Molybdenum and niobium sulphides. *Nature* 185:376–377. doi:[10.1038/185376a0](https://doi.org/10.1038/185376a0)
- [37] Fisher WG, Sienko MJ (1980) Stoichiometry, structure, and physical properties of niobium disulfide. *Inorg Chem* 19:39–43. doi:[10.1021/ic50203a009](https://doi.org/10.1021/ic50203a009)
- [38] Dash JK, Chen L, Dinolfo PH et al (2015) A method toward fabricating semiconducting 3R-NbS₂ ultrathin films. *J Phys Chem C* 119:19763–19771. doi:[10.1021/acs.jpcc.5b04057](https://doi.org/10.1021/acs.jpcc.5b04057)
- [39] Jellinek F (1962) The system tantalum-sulfur. *J Less Common Met* 4:9–15. doi:[10.1016/0022-5088\(62\)90053-X](https://doi.org/10.1016/0022-5088(62)90053-X)
- [40] Dyer C, Hendra PJ, Forsling W, Ranheimer M (1993) Surface hydration of aqueous γ -Al₂O₃ studied by Fourier transform Raman and infrared spectroscopy—I. Initial results. *Spectrochim Acta Part A Mol Spectrosc* 49:691–705. doi:[10.1016/0584-8539\(93\)80092-O](https://doi.org/10.1016/0584-8539(93)80092-O)
- [41] Nakashima S, Tokuda Y, Mitsuishi A et al (1982) Raman scattering from 2H-NbS₂ and intercalated NbS₂. *Solid State Commun* 42:601–604. doi:[10.1016/0038-1098\(82\)90617-2](https://doi.org/10.1016/0038-1098(82)90617-2)
- [42] Zhao S, Hotta T, Koretsune T et al (2016) Two-dimensional metallic NbS₂: growth, optical identification and transport properties. *2D Mater* 3:25027. doi:[10.1088/2053-1583/3/2/025027](https://doi.org/10.1088/2053-1583/3/2/025027)
- [43] Hirata T, Ohuchi F (2001) Temperature dependence of the Raman spectra of 1T-TaS₂. *Solid State Commun* 117:361–364. doi:[10.1016/S0038-1098\(00\)00468-3](https://doi.org/10.1016/S0038-1098(00)00468-3)
- [44] Duffey JR, Kirby RD, Coleman RV (1976) Raman scattering from 1T-TaS₂. *Solid State Commun* 20:617–621. doi:[10.1016/0038-1098\(76\)91073-5](https://doi.org/10.1016/0038-1098(76)91073-5)
- [45] Sugai S, Murase K, Uchida S, Tanaka S (1981) Studies of lattice dynamics in 2H-TaS₂ by Raman scattering. *Solid State Commun* 40:399–401. doi:[10.1016/0038-1098\(81\)90847-4](https://doi.org/10.1016/0038-1098(81)90847-4)
- [46] Luican-Mayer A, Guest JR, Hla S-W (2015) Suppression of charge density wave phases in ultrathin 1T-TaS₂. In: [arXiv: 1506.04102](https://arxiv.org/abs/1506.04102). <http://arxiv.org/abs/1506.04102>. Accessed 29 Oct 2016